

Supplemental Material

Decelerated Hot Carrier Cooling in Graphene *via* Nondissipative Carrier Injection from MoS₂

Minh Dao Tran^{†,‡,¶}, Sung-Gyu Lee^{†,‡,¶}, Sunam Jeon[‡], Sung-Tae Kim^{†,‡}, Hyun Kim[†], Van Luan Nguyen[†], Subash Adhikari^{†,‡}, Sungjong Woo[§], Hee Chul Park[§], Youngkuk Kim^{†,‡,*}, Ji-Hee Kim^{†,‡,*} and Young Hee Lee^{†,‡,‡,*}

Correspondence to: youngkuk@skku.edu, kimj@skku.edu, leeyoung@skku.edu

S1. Photoluminescence (PL) and absorption spectra of bare MoS₂ and MoS₂/graphene

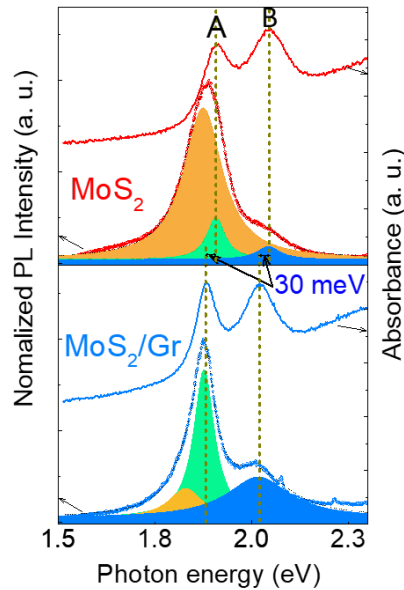


Figure S1. The PL and absorption spectra of the bare MoS₂ and the MoS₂/graphene on sapphire substrate.

Figure S1 shows the PL and absorption spectra of the bare MoS₂ (top panel) and the MoS₂/graphene heterostructure (bottom panel) on the sapphire substrate. Both PL and absorption spectra exhibit a relative redshift of A and B exciton peaks of MoS₂ in the heterostructure in comparison to those of the bare MoS₂ because of band gap renormalization from dielectric screen effect of graphene.

S2. Strain and charge doping in the MoS₂/graphene heterostructure

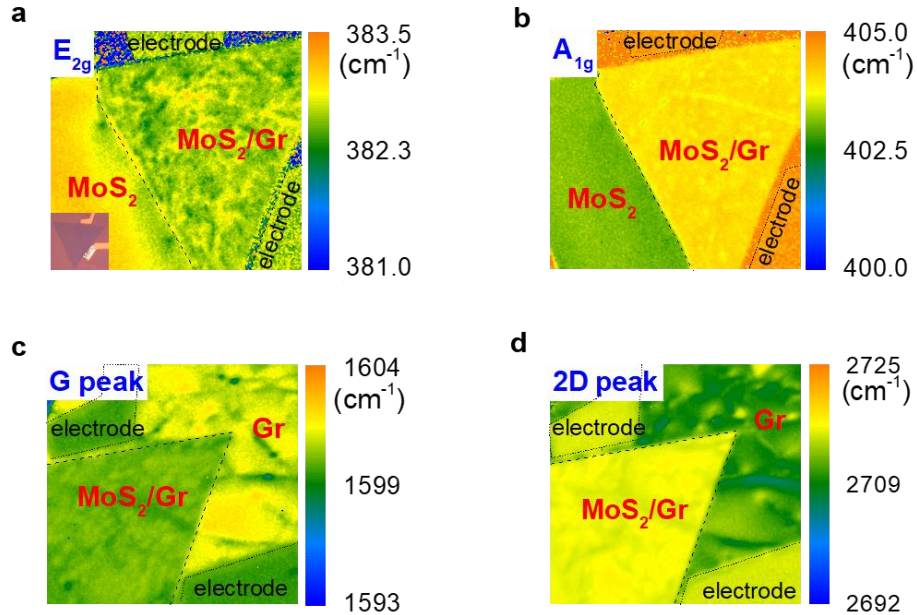


Figure S2. Strain and doping in the MoS₂/graphene heterostructure. (a, b) Peak position map of E_{2g} and A_{1g} Raman modes of the bare MoS₂ and the MoS₂/graphene heterostructure, respectively. The inset is optical image of sample. (c, d) Maps of G and 2D peak position of the bare graphene and the MoS₂/graphene regions, respectively.

Figure S2a depicts the schematic of heterostacked triangular monolayer MoS₂ on the hexagonal graphene on the SiO₂/Si substrate. Interlayer charge transfer, strain, and coupling strength in the MoS₂/graphene heterostructure were examined by confocal Raman mappings. Compared to bare MoS₂, the MoS₂ in the heterostructure exhibits a red-shift in E_{2g} peak by tensile strain¹⁻³ and a blue-shift in A_{1g} peak because of electron transfer from MoS₂ to graphene^{4,5} (figure 1b and 1c). The frequency mapping was also performed for G and 2D modes of graphene (figure 1d and 1e). In comparison to bare graphene, the G mode of graphene in the heterostructure is softened dominantly by electron withdrawing from MoS₂, while the 2D mode is hardened mostly by compressive strain, which is in line with previous reports.⁶

S3. Photo-induced electron transfer from MoS₂ to graphene in MoS₂/graphene heterostructure

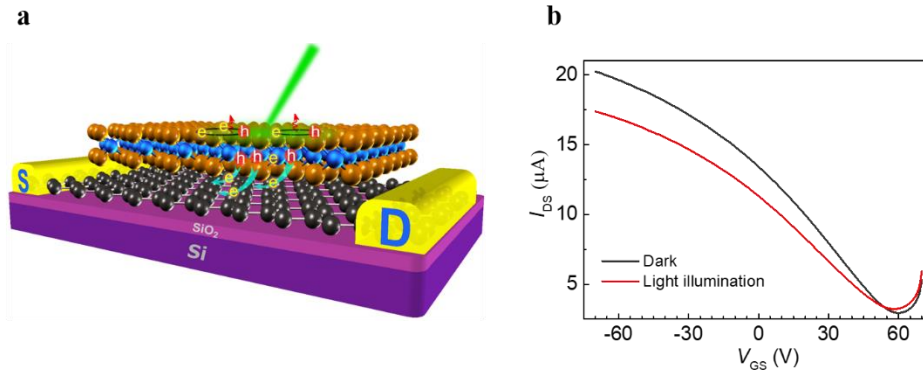


Figure S3. Photo-induced electron transfer in MoS₂/graphene heterostructure. (a) Schematic of vertical MoS₂/graphene-FET device on SiO₂/Si substrate (source, drain electrodes contact only to graphene). (b) Transfer curves of bottom graphene with (red) and without (black) light illumination, respectively.

Figure S3a illustrates the photocurrent measurement for FET-based MoS₂/graphene heterostructure as a function of gate bias. The dark I_{DS} - V_{GS} curve (black curve in figure S3b) exhibits a typical p -type of graphene with a charge-neutrality point (CNP) of ~ 60 V, equivalent to an initial hole doping concentration of $4.5 \times 10^{12} \text{ cm}^{-2}$. Under illumination of a green laser (532 nm) with a photoexcitation power of $300 \mu\text{W}$, the I_{DS} - V_{GS} curve (red trace) had a similar shape to the one obtained in the dark (black trace). It shows a pronounced drop of the illuminated I_{DS} in left side of CNP and became smaller as the gate bias approached the CNP, which indicating photogenerated electrons from MoS₂ added to the electrons in graphene. This is consistent with aforementioned Raman results.

S4. PL mapping of bare MoS₂ and MoS₂/graphene on SiO₂/Si substrate

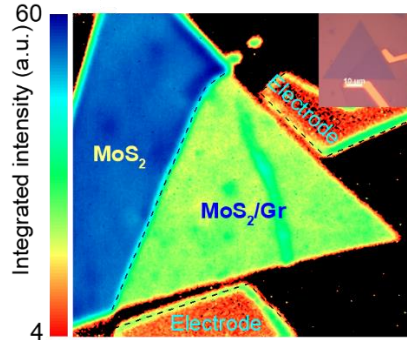


Figure S4. The quenching in PL of MoS₂ in the heterostructure. The PL mapping image of bare MoS₂ and MoS₂/graphene on SiO₂/Si substrate. The inset is optical image of sample.

S5. Presentative DT spectra of bare MoS₂, graphene and MoS₂/graphene with NIR probe

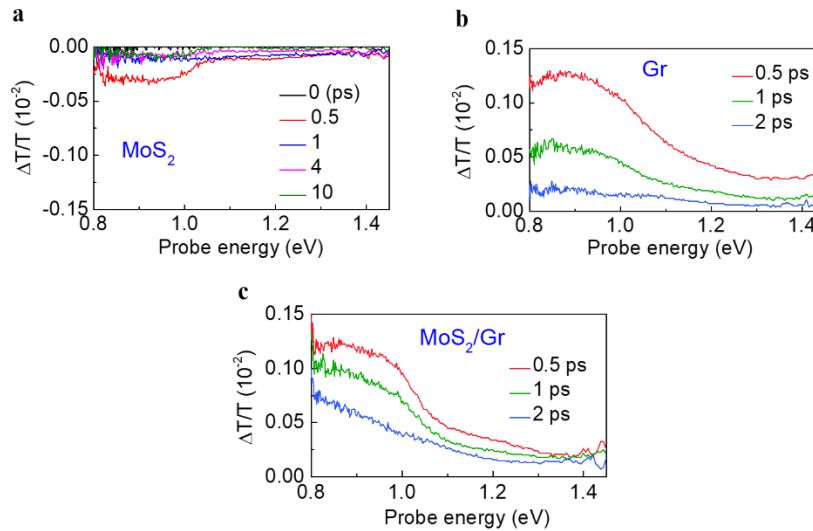


Figure S5. Different delay time DT spectra with NIR probe pulse of (a) bare MoS₂, (b) graphene, and (c) MoS₂/graphene heterostructure.

S6. Comparing NIR-TDT spectra of bare graphene and graphene of the MoS₂/graphene HS at different delay time

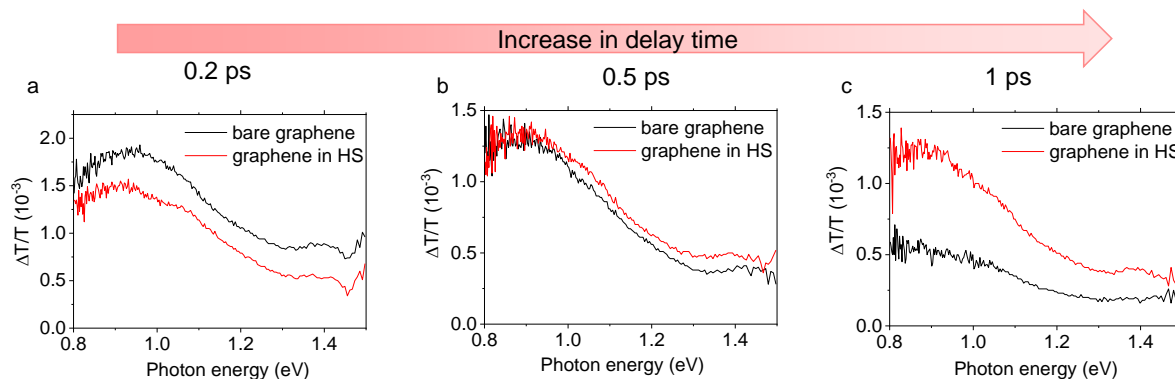


Figure S6. TDT spectra of bare graphene (black) and graphene in the HS (red) obtained at different delay times (a) 0.2 ps, (b) 0.5 ps, and (c) 1 ps.

S7. DT spectra of graphene and MoS₂/graphene with NIR probe and pumping of 1.87 eV

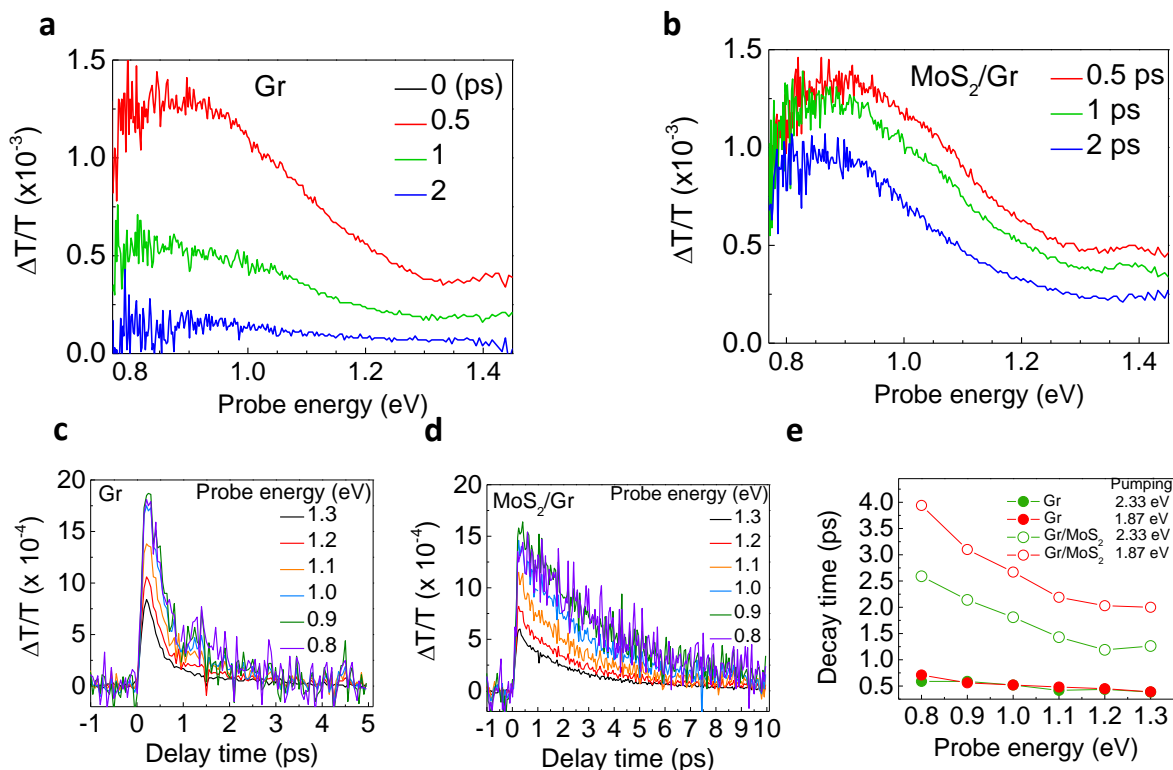


Figure S7. DT spectra probed at delay times of 0.5, 1 and 2 ps for (a) Gr and (b) MoS₂/Gr with photoexcitation at 1.87 eV. (c, d) Transient absorption dynamics at different probe energies from 0.8 to 1.3 eV for Gr and MoS₂/Gr heterostructure, respectively. (e) Probe energy dependent carrier lifetimes of Gr and MoS₂/Gr at pumping energies of 2.33 eV (non-resonant) and 1.87 eV(resonant).

S8. First-principles calculations to support that the interlayer charge transfer prolongs the carrier lifetime in MoS₂/graphene heterostructure

S8.1. Computational Methods

Our first-principles calculations were performed based on density functional theory (DFT) as implemented in the Quantum Espresso package.⁷ We used generalized gradient approximation (GGA) with the Perdew–Burke–Ernzerhof (PBE) functional.⁸ The cutoff energy for the plane wave basis is set to 816 eV. The norm-conserving, optimized, designed nonlocal pseudopotentials were generated by OPIUM.⁹ The lattice parameters and atomic positions of unit cells of graphene and MoS₂ were fully relaxed until the pressures and forces are less than 5×10^{-1} Kbar and 2.6×10^{-5} eV/Å. The two-dimensional structure of graphene and MoS₂, are modeled by constructing a supercell that places 30 Å vacuum. To obtain a self-consistent charge density, we sampled 6×6 and 30×30 k points in the first Brillouin zone using the Monkhorst–Pack method¹⁰ for the heterostructure and unit cells, respectively. The graphene/MoS₂ heterostructure is modeled by a supercell comprising 5×5 and 4×4 graphene and MoS₂ primitive unit cells, respectively. The internal atomic structure in the supercell is fully relaxed until the forces are converged to $\times 10^{-5}$ eV/Å. The van der Waals interaction is considered using the DFT–D method.^{11,12} The Monkhorst–Pack $300 \times 300 \times 1$ ($60 \times 60 \times 1$) grid is used to sample the k -point of the two-dimensional Brillouin zone for the absorption coefficient calculations in graphene and MoS₂ (graphene/MoS₂ heterostructure). The broadening is set to 3000 K when calculating the optical constants.

S8.2. Optical properties

We used the linear response theory to calculate the imaginary part of dielectric constant ϵ_2

$$\epsilon_2(\omega)^{GGA} = \frac{16\pi e^2}{\omega^2} \sum_{c,v} |\langle v | \vec{v} | c \rangle|^2 \delta[\omega - (E_c - E_v)]$$

where ω is the angular frequency of the incident light, c and v represent the conduction and valence

bands, respectively. The real part of the dielectric constant is calculated using the Kramers–Kronig relation,

$$\epsilon_1(\omega) = 1 + \frac{2}{\pi} P \int_0^{\infty} d\omega' \frac{\omega' \epsilon_2(\omega)}{\omega'^2 - \omega^2}.$$

The absorption coefficient $\alpha(\omega)$ is calculated from the dielectric functions using

$$\alpha(\omega) = \frac{\omega}{c} \sqrt{2} \sqrt{\sqrt{\epsilon_1^2(\omega) + \epsilon_2^2(\omega)} - \epsilon_1(\omega)}.$$

The absorption ratio $A(\omega)$ is evaluated by

$$A(\omega) = 1 - \exp[-\alpha(\omega)d],$$

where d is the thickness of the graphene or MoS₂ monolayer, which we set to 3 Å for both systems. The chemical potential for graphene is set to ~ -0.3 eV, resulting in the Coulomb blocking for the photons with the energy below 0.6 eV. The initial carrier population δN is evaluated by^{13,14}

$$\delta N = \frac{F}{\hbar\omega} (1 - R(\omega)) A(\omega) [1 + R(\omega)\exp(-\alpha(\omega)d)]$$

where F is the the laser fluence that we used (1.27 mJ/cm²), and $R(\omega)$ is the reflectivity, calculated by

$$r = \frac{(1 - n)^2 + k^2}{(1 + n)^2 + k^2}.$$

Here, n and k are the refractive index and the extinction coefficient, respectively. They are calculated from the dielectric functions using

$$\epsilon_1 + i\epsilon_2 = (n + ik)^2.$$

S8.3. Atomic structures of 5x4 supercell

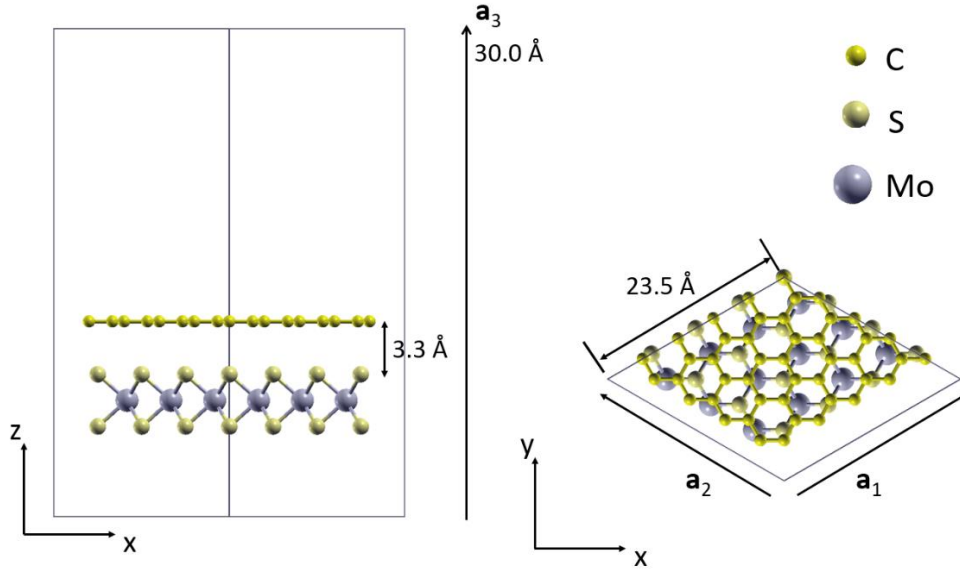


Figure S8. Atomic structure of the 5x4 supercell

To model graphene/MoS₂ heterostructure, we constructed a 5x4 supercell that contains 5x5 primitive unit cells of graphene and 4x4 primitive unit cells of MoS₂ as shown in figure S8. With respect to pristine lattice constants, a 2.5 % compressive strain is applied to MoS₂ in the supercell, while zero strain is applied to graphene.

S8. 4. Band structures of graphene/MoS₂ heterostructure

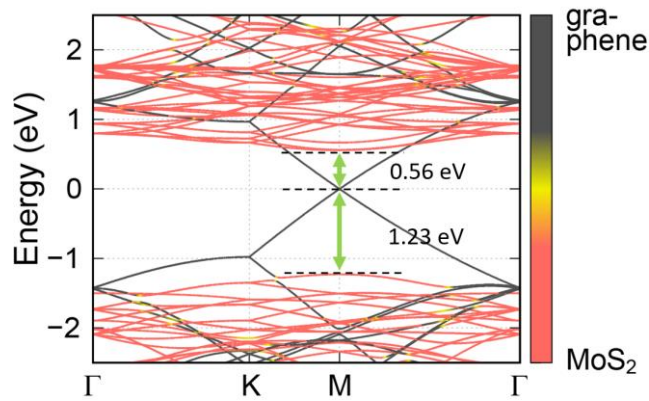


Figure S9. Electronic energy band structure of the graphene/MoS₂ heterostructure. A 5x4 supercell geometry in figure S8 is used. The grey and red lines represent the contributions from graphene and MoS₂, respectively.

Figure S9 shows the electronic energy band structure of the graphene/MoS₂ heterostructure. The heterostructure is modeled by the 5x4 supercell introduced in figure S8. The valence band maximum (conduction band minimum) of the red MoS₂ bands positions at -1.23 eV (0.56 eV) with respect to the Dirac point. The Dirac point of graphene is closer to the conduction band minimum of MoS₂ by 0.67 eV than the valence band maximum.

S8.5. Optical absorption of graphene and MoS₂

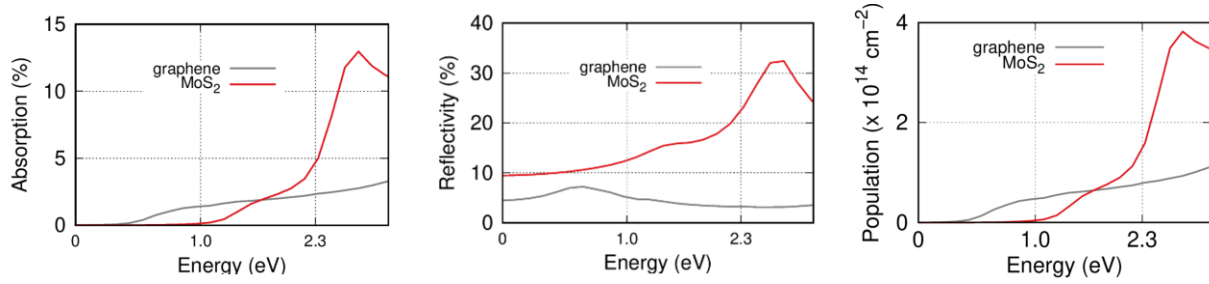


Figure S10. Optical properties and photo-excited carrier populations of graphene and MoS₂.

Figure S10 shows the calculated optical properties of graphene and MoS₂ as a function of photon energy $\hbar\omega$. Notably, we find that the single laser pulse with $\hbar\omega = 2.3 \text{ eV}$ and $F = 12.7 \text{ mJ/cm}^2$, which lasts for 80 fs, generates 0.79×10^{14} carriers in graphene and 1.7×10^{14} carriers in MoS₂ per cm^2 . If the interlayer population is negligible, around twice as many carriers are produced in MoS₂ than those in graphene.

S8.6. Interlayer charge transfer processes

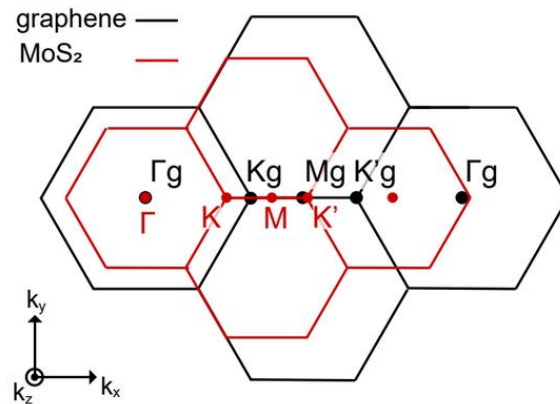


Figure S11. Incommensurate Brillouin zones of graphene (black) and MoS₂ (red).

In order to resolve the interlayer charge transfer processes, we calculate the transition intensity $|\langle k,v | p | k,c \rangle|^2$ as a function of k for the photon energy $\hbar\omega = 2.3$ eV. We present the band structure of graphene and MoS₂ along the Γ -K-M-K'- Γ of the high-symmetry momenta of MoS₂ and graphene in the incommensurate momentum space as shown in figure S11.

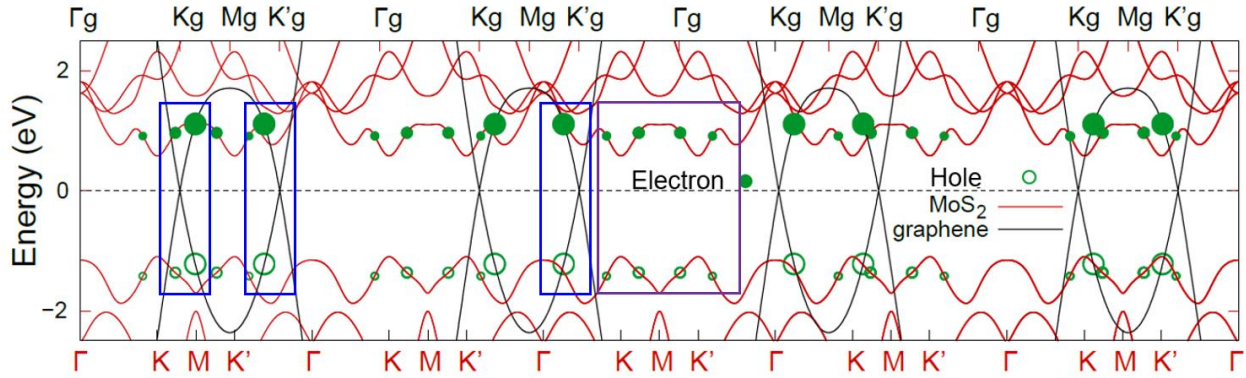


Figure S12. Electronic energy bands of graphene (black lines) and MoS₂ (red lines). Photo-excited carriers are generated at the blue circles at the photon energy of $\hbar\omega = 2.3$ eV. The size of the circle represents the transition intensity $|\langle k,v | p | k,c \rangle|^2$.

From the transition intensity plot, the hot sites, at which carriers are generated in the band structure, are identified as shown in figure S12. The hot sites are indicated by empty and filled green circles for the holes and electrons, respectively. The transition intensity is represented by the size of green circles.

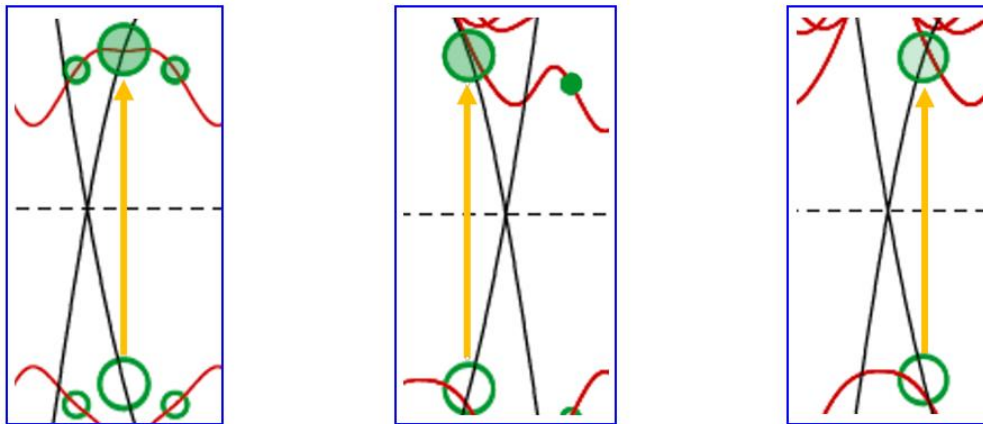


Figure S13. Photo-excitation at graphene (Magnified view of the blue boxes in the band structure in figure S12. The excitation of electrons at graphene are illustrated by yellow arrows. The photo-excited electrons of graphene are generated near the anti-crossing point

The hot carriers are initially generated either near the anti-crossing sites or beyond the anti-crossings, depending on which the interlayer charge transfer occurs in different manners. We find that the photo-excited electrons at graphene tend to occur near the anti-crossing points. This is due to the neutrality (Dirac) point of graphene that lies near the conduction band minimum of MoS₂ than the valence band maximum and the states where the photo-excited electrons arise in graphene overlap in energy with the conduction bands of MoS₂. In addition, larger density of states of MoS₂ than graphene in the conduction band region enable more chances for a conduction states of graphene to meet with a conduction state of MoS₂.

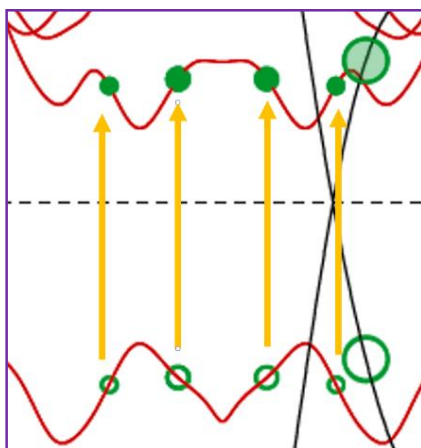


Figure S14. Photo-excitation at MoS₂ (Magnified view of the purple box in the band structure in figure S12.) The generation of photo-excited electrons at MoS₂ are illustrated by yellow arrows. The excitations occur off the anti-crossing points.

Unlike the hot electrons in graphene, the hot electrons in MoS₂ are largely generated off the anti-crossing points. This is, again, due to the fewer density of states of graphene with respect to those of MoS₂ in the conduction band region, resulting in a less chance for a MoS₂ state to coincide with a graphene state at the same lattice momentum and energy. Our calculations, thus, necessitate

the conclusion that hot electron injection from MoS₂ to graphene (from graphene to MoS₂) should be dissipative (nondissipative) with (without) the help of scattering with phonons or impurities.

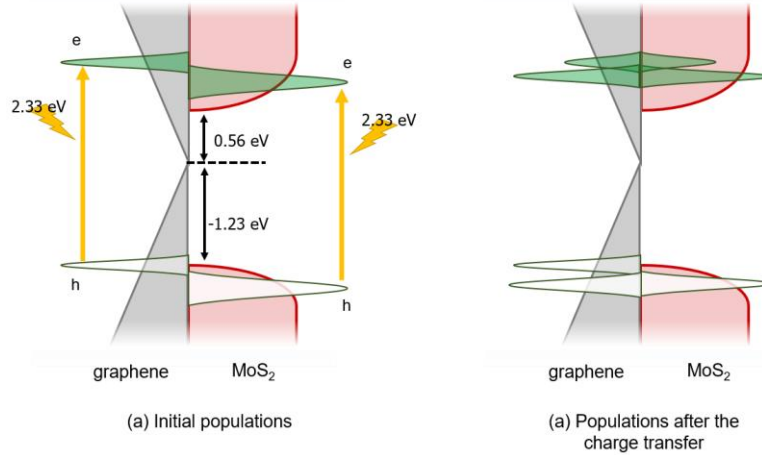


Figure S15. Schematic illustration of charge transfer between the graphene and MoS₂ layers.

Regarding the hole generation, we expect that the interlayer transfer should be dissipative irrespective of the transfer direction. For the same reasons with the hot electrons generated at MoS₂, the holes generated at MoS₂ should be dissipative; the anticrossing hot sites are rare due to the low density of states of graphene, and thus, the transfer to graphene should occur *via* scattering process of phonons or impurities. In contrast, unlike the electrons generated at graphene, the holes generated at graphene are unlikely to be transferred to MoS₂, and, if any, the process should be dissipative. This contrasting behaviors of the electrons and holes at graphene originate from the asymmetry of the graphene bands. As shown in figure S12 and S13, the hot spots of graphene where holes are generated are in the vicinity of the band gap edge of MoS₂. In order to inject the graphene holes to MoS₂, an extra gain and energy and lattice momentum is need, thus being unlikely.

The calculations show that more carriers are populated in the heterostructure than in bare graphene. MoS₂ generates around 0.91×10^{14} more electrons per cm² than graphene for a single laser pulse. Although hot carriers can transfer from one layer to the other layer, the injection of hot electrons from MoS₂ to graphene should be a more efficient process due to the anticrossing states, which dominantly appear at the MoS₂ hot sites. Similarly, while 1.7×10^{14} and 0.79×10^{14} holes are

populated initially in MoS₂ and graphene, respectively, the injection of hole-type hot carriers into graphene should be more efficient and fast from MoS₂ to graphene due to the anti-crossings. In addition, due to the asymmetry of the graphene bands in the presence of MoS₂ bands, the transfer of hole-type hot carriers to MoS₂ *via* electron–electron coupling is expected to be even more inefficient. The hot hole spots of graphene reside near or above the valence band edge of MoS₂. This should make the unbalanced injection of hole-type carriers from MoS₂ to graphene even more significant. Roughly estimating, the unbalanced hot electrons at MoS₂ will transfer to graphene, resulting in the net injection of around 0.46×10^{14} hot electrons from MoS₂ per a pulse. Regarding holes, the transfer from MoS₂ to graphene should be ultrafast, while the transfer in the other direction is unlikely to occur. Therefore, if the hole injection is one-directional from MoS₂ to graphene, around the half of the MoS₂ holes transfer to graphene, which corresponds to 0.85×10^{14} holes. In any circumstance we expect more holes are populated in graphene in the early stage of the generation.

References

- (1) Zhu, C. R.; Wang, G.; Liu, B. L.; Marie, X.; Qiao, X. F.; Zhang, X.; Wu, X. X.; Fan, H.; Tan, P. H.; Amand, T.; Urbaszek, B. Strain Tuning of Optical Emission Energy and Polarization in Monolayer and Bilayer MoS₂. *Phys. Rev. B* **2013**, *88*, 121301.
- (2) McCreary, A.; Ghosh, R.; Amani, M.; Wang, J.; Duerloo, K. N.; Sharma, A.; Jarvis, K.; Reed, E. J.; Dongare, A. M.; Banerjee, S. K.; Terrones, M.; Namburu, R. R.; Dubey, M. Effect of Uniaxial and Biaxial Strain on Few-Layered Terrace Structures of MoS₂ Grown by Vapor Transport. *ACS Nano* **2016**, *10*, 3186–3197.
- (3) Conley, H. J.; Wang, B.; Ziegler, J. I.; Haglund, R. F.; Pantelides, S. T.; Bolotin, K. I. Band gap Engineering of Strained Monolayer and Bilayer MoS₂. *Nano Lett.* **2013**, *13*, 3626–3630.
- (4) Chakraborty, B.; Bera, A.; Muthu, D. V. S.; Bhowmick, S.; Waghmare, U. V.; Sood, A. K. Symmetry-Dependent Phonon Renormalization in Monolayer MoS₂. *Phys. Rev. B* **2012**, *85*, 161403.

- (5) Miller, B.; Parzinger, E.; Vernickel, A.; Holleitner, A. W.; Wurstbauer, U. Photogating of Mono- and Few-Layer MoS₂. *Appl. Phys. Lett.* **2015**, *106*, 122103.
- (6) Liu, X.; Balla, I.; Bergeron, H.; Campbell, G. P.; Bedzyk, M. J.; Hersam, M. C. Rotationally Commensurate Growth of MoS₂ on Epitaxial Graphene. *ACS Nano* **2016**, *10*, 1067–1075.
- (7) Giannozzi, P.; Baroni, S.; Bonini, N.; Calandra, M.; Car, R.; Cavazzoni, C.; Ceresoli, D.; Chiarotti, G. L.; Cococcioni S.; Dabo, I.; Corso, A. D.; Gironcoli, S.; Fabris, S.; Fratesi, G.; Gebauer, R.; Gerstmann U.; Gougoussis, C.; Kokalj, N.; Lazzeri, M.; Martin-Samos, L.; *et al.* QUANTUM ESPRESSO: A Modular and Open Source Software Project for Quantum Simulations of Materials. *J. Phys. Condens. Matter* **2009**, *21*, 395502.
- (8) Perdew, J. P.; Zunger, A. Self-Interaction Correction to Density-Functional Approximations for Many-Electron Systems. *Phys. Rev. B* **1981**, *23*, 5048.
- (9) Rappe, A. M.; Rabe, K. M.; Kaxiras, E.; Joannopoulos, J. D. Optimized Pseudopotentials *Phys. Rev. B* **1990**, *41*, 1227.
- (10) Monkhorst, H. J.; Pack, J. D. Special Points for Brillouin-Zone Integrations. *Phys. Rev. B* **1976**, *13*, 5188.
- (11) Grimme, S. Semiempirical GGA-Type Density Functional Constructed with a Long-Range Dispersion Correction. *J. Comp. Chem.* **2006**, *27*, 1787–1799.
- (12) Barone, V.; Casarin, M.; Forrer, D.; Pavone, M.; Sambri, M.; Vittadini, A. Role and Effective Treatment of Dispersive Forces in Materials: Polyethylene and Graphite Crystals As Test Cases. *J. Comp. Chem.* **2009**, *30*, 934.
- (13) Harb, M.; Ernstorfer, R.; Dartigalongue, T.; Hebeisen, C. T.; Jordan, R. E.; Miller, R. J. D. Carrier Relaxation and Lattice Heating Dynamics in Silicon Revealed by Femtosecond Electron Diffraction. *J. Phys. Chem. B* **2006**, *110*, 25308.
- (14) Cushing, S. K.; Zürich, M; Kraus, P. M.; Carneiro, L. M.; Lee, A.; Chang, H. T.; Kaplan, C. J.; Leone, S. R. Hot Phonon and Carrier Relaxation in Si(100) Determined by Transient Extreme Ultraviolet Spectroscopy. *Struct. Dyn.* **2018**, *5*, 054302.